Desalination and Water Treatment
www.deswater.com
doi: 10.1080/19443994.2013.765810

51 (2013) 6498–6506
October

Taylor & Francis
Taylor & Francis Group

Analysis of brine desalination with different channels by vacuum membrane distillation

Li Xin*, Gao Donglin, Liu Jia

School of Chemical Engineering and Environment, Beijing Institute of Technology, Beijing, China
Tel. +86-68918978; email: klkxlx@163.com

Received 13 November 2012; Accepted 8 January 2013

ABSTRACT

The fluid flow in a rectangular channel is observed by a high-speed fluid field display system, and the fluid appearances under different operate parameters are presented pictorially. Numerical simulations are performed to investigate brine desalination by vacuum membrane distillation (VMD) with three different channel configurations (rectangular, serpentine and spiral) to compare the effect of channel configuration on the process. The results obtained from simulation are analysed from the viewpoint of field synergy. This study concludes that better field synergy leads to better membrane permeability flux. The spiral channel shows the best performance in enhancing heat transfer and increasing the synergy. Increasing the co-direction component of the multi-field could enhance the transfer process. The numerical simulation results are consistent with experimental results.

Keywords: Vacuum membrane distillation; Desalination; Channel configuration

1. Introduction

Vacuum membrane distillation (VMD), a membrane distillation (MD) process, has become an active area of research with the characteristics of high thermal efficiency and large mass transfer flux. VMD has potential application as a frequently used technique for separating dilute aqueous mixtures, for example, in the treatment of water coloured with methylene blue dye [1], the treatment of dye solutions [2] and the removal of ammonia from aqueous solution [3]. VMD has also been applied to separate and concentrate heat-sensitive materials (juice, herbs, etc.). For example, the concentration of sucrose solutions [4] and ginseng extract aqueous solutions [5], brine desalination and water production by direct contact membrane [6], membrane-controlled release of a drug from a hybrid dispersed network–membrane-based system and the release of small molecules such as nico-resertine, caffeine and benzoic acid have been reported [7,8].

In recent years, brine desalination has been an important strategy for overcoming the water shortage caused by the increasing depletion of freshwater resources. Compared with traditional desalination methods (distillation and reverse osmosis (RO)), VMD is still a new separation technology. If the VMD systems couple with solar energy, the brine desalination by VMD process is feasible. The maintenance costs are from pumps [9]. However, the development of membrane technology and the emergence of new materials reflect the remarkable potential of VMD processes. Many of the published works focus on this area [10].

In particular, many works have been devoted to the numerical simulation of MD. The flows of cold

*Corresponding author.

and hot solution were simulated by Alklaibi et al [11,12] using the finite element method to simulate air gap membrane distillation (AGMD) and direct contact membrane distillation (DCMD) processes, which were modelled as a two-dimensional conjugate problem. The model couples the continuity, momentum, energy and species conservation equations of the feed and cold solution. The transport of the vapour through the membrane was described by molecular diffusion. The effects of the main operating parameters and membrane parameters on the permeability flux were also analysed in the MD process. Qtaishat et al. [13] proposed a heat transfer model for DCMD brine treatment. The details of all heat transfer mechanisms in the feed stream were illustrated, and the heat transfer was divided into three regions: the feed solution thermal boundary layer, the membrane and the permeate solution thermal boundary layer. Simple energy and mass balances were proposed with a system of non-linear equations using a number of unknowns. The permeate stream was based on the direct experimental observation of heat and mass fluxes. The heat transfer equations were solved using the FSOLVE functions in MATLAB.

To date, many theoretical and experimental works have been performed to enhance the transfer process to save energy. Meanwhile, improving production efficiency is also an important research topic for researchers. By considering an analogy between heat convection and heat conduction with heat source, Guo et al. [14,15] studied the mechanisms of convective heat transfer and proposed a novel concept regarding the enhancement of convective heat transfer for a parabolic fluid. They found that the strength of the heat source not only depended on the fluid properties and velocity but was also synergistically related to the velocity and temperature gradient vectors. The relationship between the velocity and heat flux vectors had a significant impact on heat transfer. The improvement of the coordination of velocity field and temperature field could enhance heat transfer, which is referred to as the field synergy principle. This principle thus reveals the physical nature of the convection heat transfer and heat transfer enhancement. A series of new methods for controlling the strength of convective heat transfer were developed.

The fluid flow in the membrane module usually cannot be observed visually. To observe the actual fluid flow, a high-speed field display system is used to image the fluid in the membrane module. Based on the established geometric model of a flat membrane module with different channel configurations, brine desalination via VMD was simulated. The simulation results for three different flow channels (rectangular, serpentine and spiral) were compared and analysed from the viewpoint of the field synergy principle.

2. Experiment

The high-speed fluid field display system includes several units: a polymethyl methacrylate membrane module, high-speed camera, computer and dysprosium light source. A HG-LE high-speed camera (phantom V7.3, VRI Company, American) is used with a CMOS sensor as the recording medium. A dysprosium light source (1,000 W) is used as the main lighting and auxiliary illuminant. Red ink is used to mark the fluid flow path. The fluid field display system is shown in Fig. 1. All units are set up in the appropriate position, and the observation angle is adjusted include the fluid in the module. In the experiment, red ink is injected into the feed solution at the entrance. The fluid is captured by the high-speed camera, and the pictures are recorded and processed using a computer, it can be seen the changes from the pictures due to the change of process conditions.

3. Model description

The VMD process in the membrane module is depicted in Fig. 2(a). The feed solution is pumped into the membrane module. Some of the volatile components evaporated from the hot side of the membrane surface. Because of the membrane hydrophobicity, as long as the pressure difference across the membrane is not greater than the liquid osmotic pressure, the liquid does not pass through the membrane pore. The vacuum device maintains a pressure on the cold side that is below the equilibrium vapour pressure of the volatile components, which causes the vapour to

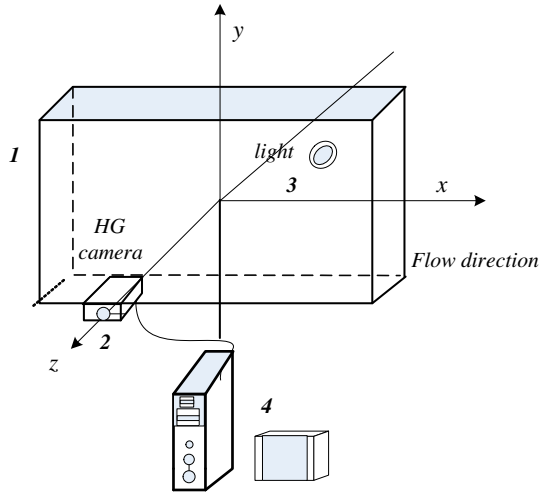

Fig. 1. High-speed fluid field display system.

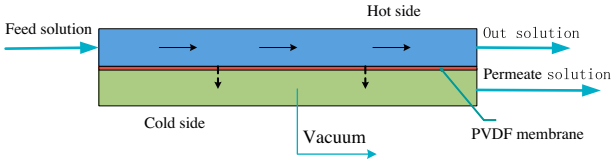

(a) Schematic diagram of the membrane distillation process in the module

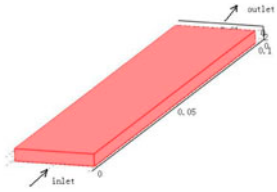

(b)

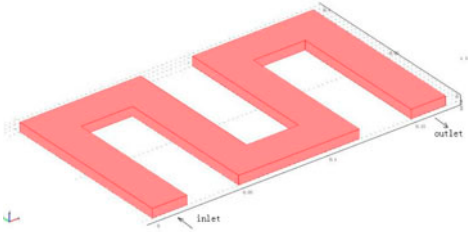

(c)

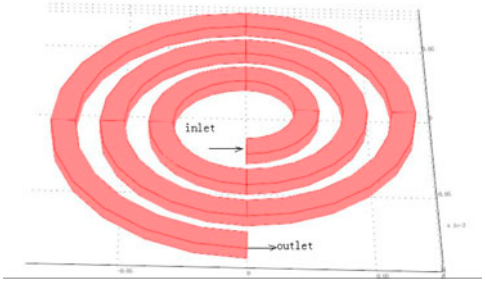

(d)

Fig. 2. Schematic diagram of the VMD process and geometry of the flow channels.

Table 1
Characteristic of PVDF Membrane

Material	PVDF
Nominal pore size, m	0.2
Thickness, mm	0.2
Porosity,%	41.2
Manufacturer	Millipore

pass through the membrane into cold side due to the pressure difference. The membrane used in this study is a polyvinylidene fluoride (PVDF) microporous hydrophobic membrane, and the relevant physical parameters are given in Table 1.

The models for VMD include heat and mass transfer. To simulate the fluid flow in the module, 3D geometric models are created for the rectangular, serpentine and spiral channels. The rectangular model is 0.1 m long, 0.02 m wide and 0.003 m deep, as shown in Fig. 2(b). The serpentine channel is 0.17 m long, 0.02 m wide and 0.003 m deep, as shown in Fig. 2(c). The spiral channel is 0.02 m wide and 0.003 m deep, the radius of spiral channel is 0.08 m, as shown in Fig. 2.

In the analysis of VMD, the governing equations for the solution coupled the continuity, momentum, energy and species conservation equations of the feed and cold solutions. For any fluid flow system, momentum conservation is the most fundamental law. According to the law of momentum conservation, the fluid momentum conservation equations for the x, y, z direction are shown as follows:

$$u\frac{\partial u}{\partial x}+v\frac{\partial u}{\partial y}+w\frac{\partial u}{\partial z}=-\frac{1}{\rho}\frac{\partial p}{\partial x}+\frac{\eta}{\rho}\left(\frac{\partial^2 u}{\partial x^2}+\frac{\partial^2 u}{\partial y^2}+\frac{\partial^2 u}{\partial z^2}\right)+Fx \tag{1}$$

$$u\frac{\partial v}{\partial x}+v\frac{\partial v}{\partial y}+w\frac{\partial v}{\partial z}=-\frac{1}{\rho}\frac{\partial p}{\partial x}+\frac{\eta}{\rho}\left(\frac{\partial^2 v}{\partial x^2}+\frac{\partial^2 v}{\partial y^2}+\frac{\partial^2 v}{\partial z^2}\right)+Fy \tag{2}$$

$$u\frac{\partial w}{\partial x}+v\frac{\partial w}{\partial y}+w\frac{\partial w}{\partial z}=-\frac{1}{\rho}\frac{\partial p}{\partial x}+\frac{\eta}{\rho}\left(\frac{\partial^2 w}{\partial x^2}+\frac{\partial^2 w}{\partial y^2}+\frac{\partial^2 w}{\partial z^2}\right)+Fz \tag{3}$$

The fluid must satisfy mass transfer conservation and energy conservation, and equations of which are as follows. It is assumed that the heat lost to the surroundings is negligible, channel walls are defined no sliding boundary conditions, porous channel is isotropic homogeneous medium. Inlet fluid is assumed to continuum mechanics.

$$\frac{\partial u}{\partial x}+\frac{\partial v}{\partial y}+\frac{\partial w}{\partial z}=0 \tag{4}$$

$$\frac{\partial(\rho T)}{\partial t}+\frac{\partial(\rho uT)}{\partial t}+\frac{\partial(\rho vT)}{\partial t}+\frac{\partial(\rho wT)}{\partial t}=\frac{\partial}{\partial x}\left(\frac{k}{cP}\frac{\partial T}{\partial x}\right)+\frac{\partial}{\partial x}\left(\frac{k}{cP}\frac{\partial T}{\partial y}\right)+\frac{\partial}{\partial x}\left(\frac{k}{cP}\frac{\partial T}{\partial z}\right)+ST \tag{5}$$

$$S_T=(\eta u_i+C_r\frac{1}{2}\rho\mid u_i\mid u_i) \tag{6}$$

The boundary conditions are provided as follows: Inlet: $u=u_0,\ c=c_0,\ T=T_0$ Outlet: $\vec{n}\cdot(-k\nabla T)=0$, $\vec{n}\cdot(-D\nabla c)=0, P=0$. The thermal conductivity

coefficient of brine is a slightly higher than that of pure water and decreases somewhat with increasing salinity. In the simulation, the thermal conductivity of brine is replaced with that of pure water, incurring an error of less than 5%. The relation between the thermal conductivity of pure water and temperature is shown in Fig. 3.

The operation temperature of the system ranged from 313 to 353 K, and the thermal conductivity could be obtained as follows:

$$k = 9.8 \times 10^{-4} T + 0.99031 \tag{7}$$

Schofield [13] put forward three mass transfer modes according to the relative sizes of the gas molecule free path and membrane pore: Knudsen diffusion, molecule diffusion and Poiseuille flow. The diffusion mechanism through the membrane in MD is determined by the molecular free path and the membrane pore size d.

The molecular free path is calculated by the followed equation [13]:

$$\lambda = \frac{K_B T}{P\sqrt{2}\pi\sigma^2} \tag{8}$$

When membrane pores are small and the vapour density is low, the pore size is far less than the gas molecule free path. Relative to collisions between gas molecules and the inner wall of the porous membrane, the collisions of molecules can be ignored.

The diameter of the membrane pore was 0.2 m, $d \leqslant 0.05\lambda$, and the diffusion mechanism in the mass transfer process through the membrane is described by Knudsen diffusion. Neglecting the collisions of molecules, the diffusion coefficient could be expressed as K_m:

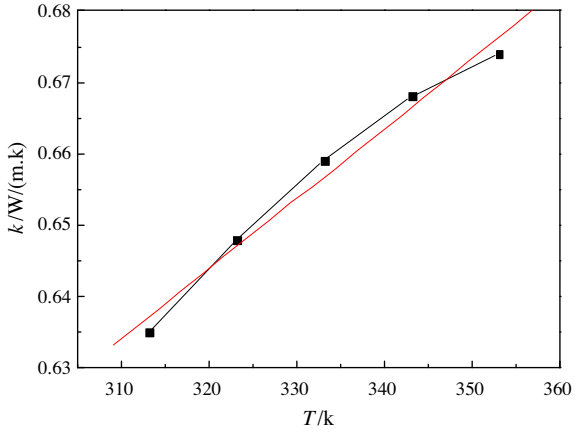

Fig. 3. The relation between the thermal conductivity of pure water and temperature.

$$K_m = 1.064 \frac{r\varepsilon}{\tau\delta}\left(\frac{M}{RT_m}\right)^{1/2} \tag{9}$$

Using the method of iteration, multi-field coupling models are solved by the UMFPACK resolver in the COMSOL. The solutions of the coupled momentum and energy conservation equations are used to solve the concentration field. The membrane permeability flux profile is a mean permeability flux.

4. Results and discussion

4.1. Fluid flow in the membrane module

On the cold side, the vacuum is 0.090 MPa, the feed liquid concentration is 5 g/L, the feed liquid concentration is 323 K, and the feed rate is 50 L/h. The transient fluid flow is recorded by a high-speed camera. The pictures for different times are shown in Fig. 4. These pictures show that the fluid velocity in the centre area is larger than the boundary velocity, which is consistent with fluid mechanics theory. These fluid flow pictures provide a visual representation of this phenomenon. The effect of feed temperature and feed flow rate is investigated.

The fluid flow is dependent on the feed temperature. Fig. 5 presents the fluid flow pictures at 318 and 338 K for the same point in time, a feed liquid concentration of 5 g/L, a vacuum degree of 0.090 MPa, and a feed rate of 150 L/h. The higher temperature corresponds to increased fluid diffusion.

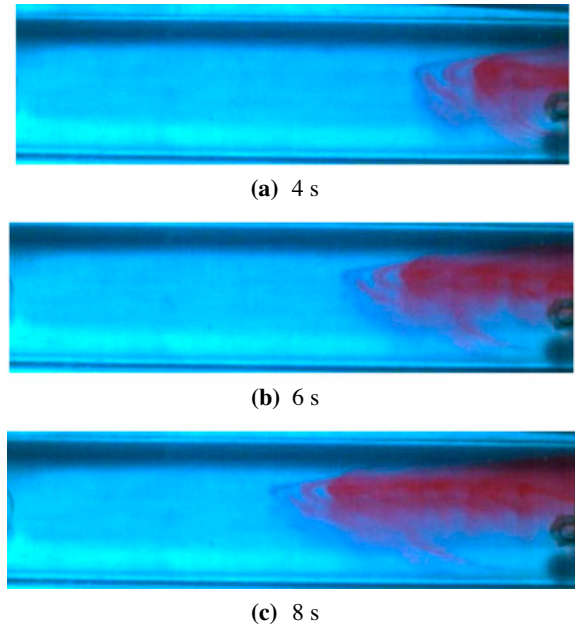

(a) 4 s

(b) 6 s

(c) 8 s

Fig. 4. Fluid flow at different times (a) 4 s, (b) 6 s, and (c) 8 s.

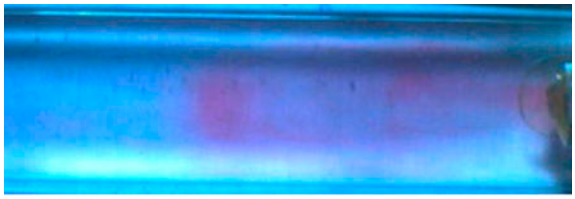

(a) 318 K

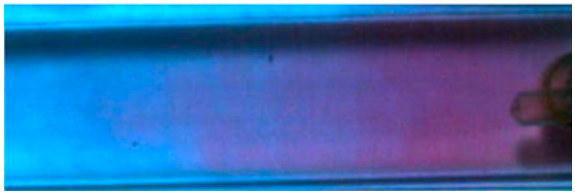

(b) 338 K

Fig. 5. Fluid flow at different temperatures (a) 318 K and (b) 338 K.

(a) 50 L/h

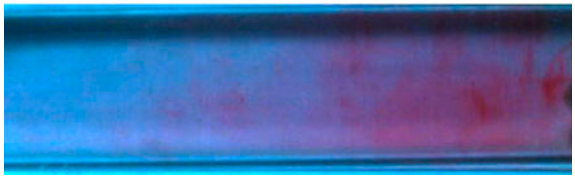

(c) 250 L/h

Fig. 6. Fluid flow at different temperatures (a) 50 L/h and (b) 250 L/h.

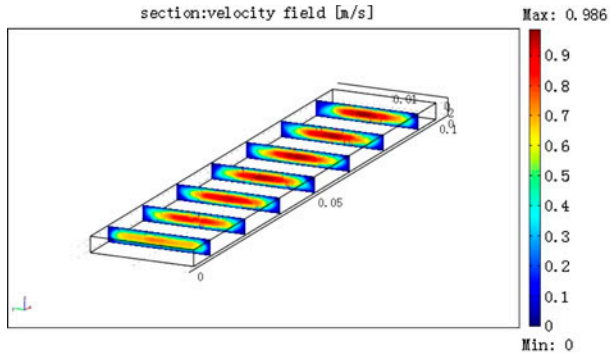

(a) Velocity field section of the rectangular channel

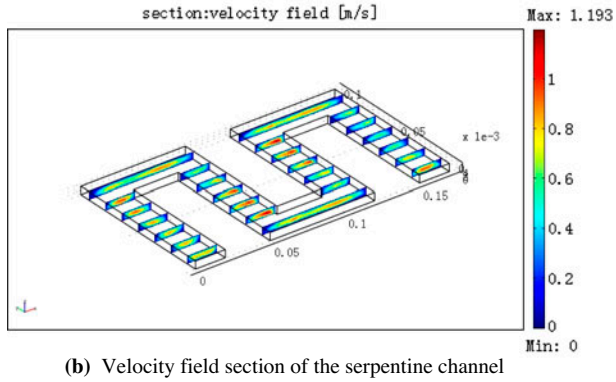

(b) Velocity field section of the serpentine channel

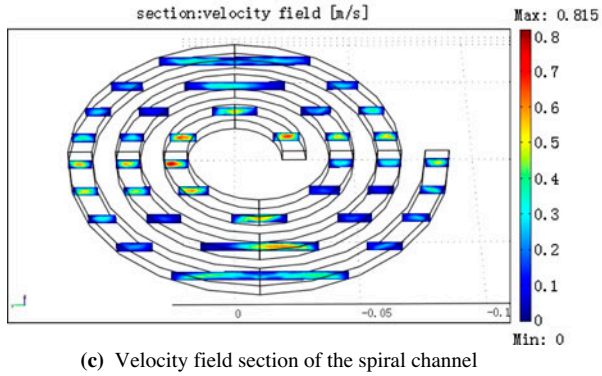

(c) Velocity field section of the spiral channel

Fig. 7. Velocity field sections of the three channels (a) Velocity field section of the rectangular channel (b) Velocity field section of the serpentine channel (c) Velocity field section of the spiral channel.

The feed flow rate significantly changes the fluid velocity distribution and disorder degree. As shown in Fig. 6, the turbulence increases with feed flow rate, which improves mass transfer and heat transfer, the membrane permeability flux increases.

4.2. Velocity field analysis

The inlet flow rate is set to 0.6 m/s and the temperature is set to 323 K. The velocity field for the three channels is depicted in Fig. 7. An obvious difference is observed between the central and non-central regions in the distribution of the velocity field. In each section, the speed is highest when the fluid is closer to the central area, which is consistent with the pictures in Fig. 4.

4.3. Temperature field analysis

The temperature field distribution of the module is shown in Fig. 8. The temperature decreased gradually from the entrance to the exit of the flow channel because the heat loss increases closer to the exit. The temperature changes across the region are approximately 2 K. In the rectangular channel, as shown in Fig. 8(a), the temperature in the central region was higher than the temperature on either side, and the

temperature is different in each region. As shown in Fig. 8(b) and Fig. 8(c), the temperature field in the first section of the serpentine and spiral channels was the same as that in the rectangular channel; however, the temperature eventually obtains a constant value later in the serpentine and spiral channels. Because of the short flow duration through the rectangular channel, the temperature cannot become constant. The serpentine and spiral channels are longer than the rectangular channel, which allows the temperature to become constant in later sections.

4.4. Concentration field analysis

The concentration field distributions of the three channels are given in Fig. 9; the changes in the concentration fields differ for each flow channel. The concentration change is not very clear for the rectangular channel, as shown in Fig. 9(a). Due to the small concentration diffusion coefficient and the small amount of water vapour moving through the membrane pore, only the local concentration could be changed. In the serpentine channel, it is evident each

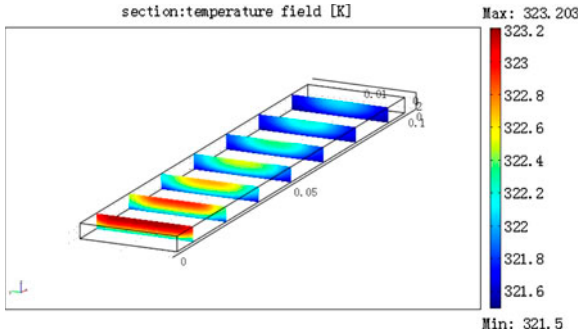

(a) Temperature field of the rectangular channel

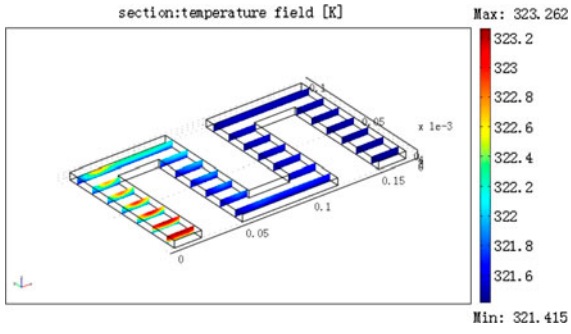

(b) Temperature field of the serpentine channel

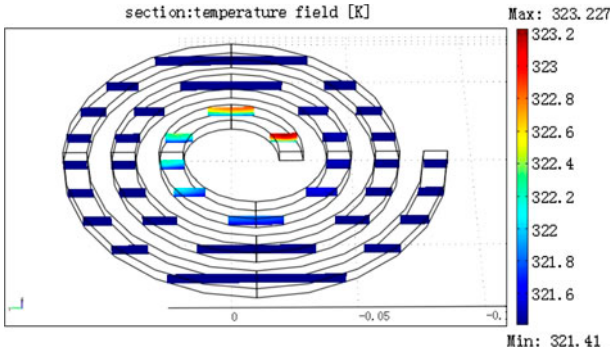

(c) Temperature field of the spiral channel

Fig. 8. Temperature fields of the three channels (a) Temperature field of the rectangular channel (b) Temperature field of the serpentine channel (c) Temperature field of the spiral channel.

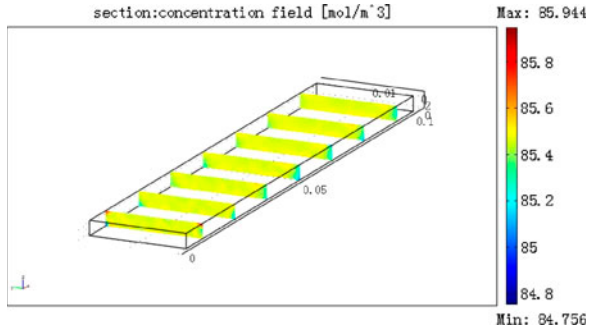

(a) Concentration field of the rectangular channel

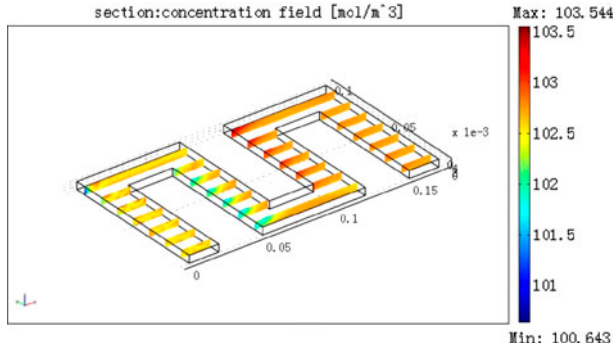

(b) Concentration field of the serpentine channel

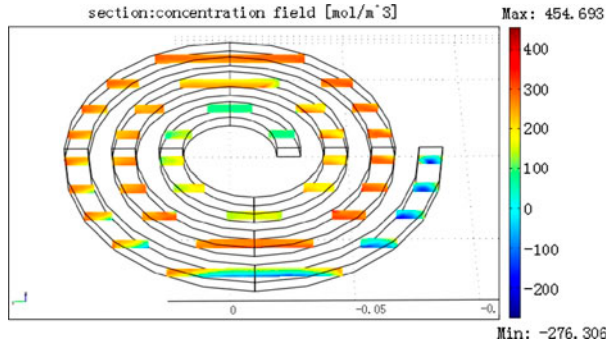

(c) Concentration field of the spiral channel

Fig. 9. Concentration fields of the three channels (a) Concentration field of the rectangular channel (b) Concentration field of the serpentine channel (c) Concentration field of the spiral channel.

section is slightly different, with the concentration increasing gradually overall from the entrance to the exit, as shown in Fig. 9(b). The largest concentration change is exhibited by the spiral channel, in which the concentrations in the inlet and outlet regions are slightly lower than that in the other regions.

4.5. Comparison of simulation and experimental results

Using a PVDF membrane, the rectangular channel module is selected for experimental study with a the feed concentration of 5 g/L and a vacuum of 0.090 MPa in the feed temperature range of 318–338 K [16]. The comparison of the experimental results and the results of the numerical simulation is shown in Figure 10, in which the experimental and simulation results are represented by the black and red lines, respectively. At a high feed flow rate, the membrane flux increases significantly with increasing temperature. The pressure at the hot side increases as the temperature increases; thus, both the mass transfer of water vapour through the membrane and the membrane flux increase. Based on the information presented in this figure, the simulation results are in accordance with the general trends exhibited by the experimental results.

4.6. Field synergy analysis and channel comparison

The field synergy principle, which is different from the traditional enhancement methods, focuses on the multi-field synergy and enhances heat transfer by increasing the synergy. The multi-field cosine represents the field synergy to some extent and can be expressed as [12]

$$\cos\beta = \frac{\overline{U}\nabla\overline{T}}{|\overline{U}||\nabla\overline{T}|} \tag{10}$$

As the indicator describing the field synergy, the value of $\cos\beta$ is between 0 and 1. Thus, the field achieves full coordination when β is 0° and there is no synergy when β was 90°.

It should be noted that no chemical reaction occurred during the VMD brine desalination. In addition, the coupling of mass and heat transfer cannot be ignored in the interaction of simultaneous mass and heat transfer. In general, increasing the driving force and reducing the resistance are used to enhance the transfer process of VMD. The synergy of the velocity and temperature field can enhance heat transfer. The pressure increase on the membrane surface increases the co-direction component and the heat transfer rate. Thus, the membrane separation performance would be enhanced.

The field synergy principle is employed to analyse the simulation results of different flow channels in this work. Under the same process conditions, the variation of the synergy with Reynolds number between the temperature and flow field in three flow channels (rectangular, serpentine and spiral) is shown in Fig. 11.

The figure illustrates that the synergy of each flow channel changed little with increasing Reynolds number. In contrast, the synergy varied strongly by flow channel shape, with the spiral channel having the greatest synergy and the rectangular channel having the least synergy. Therefore, under the same process conditions, the synergy degree between the velocity vector and the temperature gradient in the spiral flow channel is greater than that of the other channels.

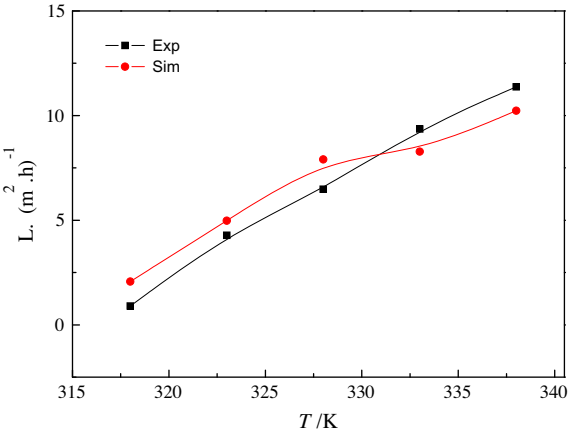

Fig. 10. Comparison of experimental and simulation results for the water flux.

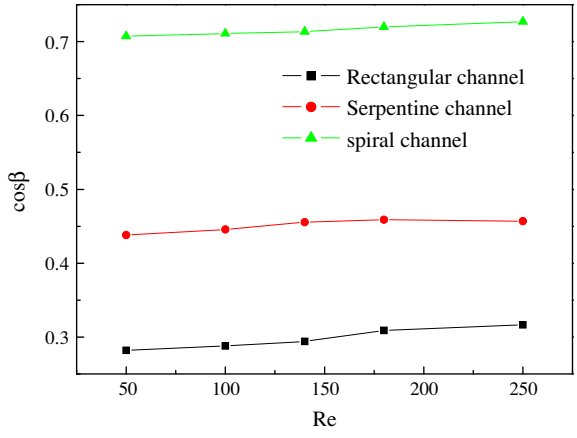

Fig. 11. Variation of the synergy with Reynolds number for three flow channels.

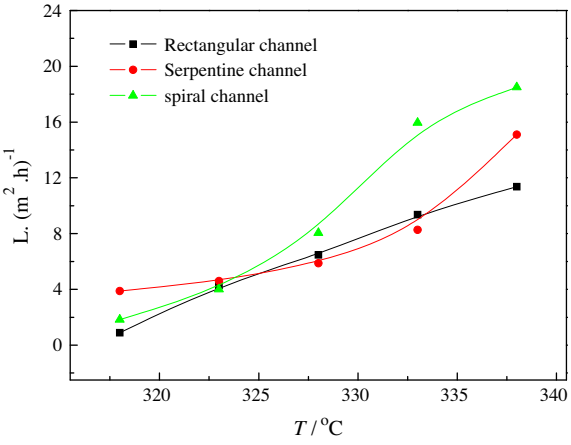

Fig. 12. Comparison of water flux for different flow channels.

The simulation results of membrane permeability flux in different flow channels are compared in Fig. 12. The three differently coloured lines in the figure represent the three different flow channel configurations: black represents the rectangular flow channel, red represents the serpentine flow channel, and green represents the spiral flow channel. Comparing the simulation results, the water flux of three channels increased with increasing initial temperature under the same process conditions. The water flux theoretically achieved maximum of 21.8 L/(m^2 h) in the rectangular channel, 24.3 L / (m^2 h) in the serpentine channel and 25.8 L/(m^2 h) in the spiral channel at the highest temperature, 343 K. The increasing tendency is similar for each channel from 318 to 328 K, whereas the water flux increases more rapidly for the spiral channel than for the other flow channels from 328 to 343 K. In addition, the water flux of the spiral channel at the maximum temperature was greater than that of the other two channels. The spiral membrane module packing density is denser and effective membrane area is larger than the other two membrane modules[17,18], the total flux should be more than the other two membrane modules.

The membrane permeability flux results are consistent with the results of the field synergy analysis: higher field synergy leads to a higher membrane permeability flux. The spiral channel configuration is the best configuration among three channels for increasing the field synergy.

Conclusion

In this paper, the fluid flow is observed using a high-speed camera, models of rectangular, serpentine and spiral flow channel are established, and brine desalination by VMD is simulated for each different channel. The simulation results, including the flow fields and flux of the three channels, are compared from a field synergy viewpoint. The fluid flow forms are presented as functions of the operation parameters. The achieved numerical simulation results are quite consistent with the experimental results, which indicates the validity of the proposed model. The simulated results confirm that the spiral flow channel enhances heat transfer and yields the best membrane permeability flux. The synergy analysis of the temperature and velocity field using the field synergy principle indicates that the synergy angle determined the synergy of the fields for otherwise identical process conditions. The heat transfer effect of different flow channels could be affected by the degree of field synergy, and the membrane permeability flux can be improved.

Nomenclature

J	—	membrane flux (L/m^{2}h)
V	—	sample volume (L)
A	—	effective membrane area (m^2)
t	—	sample time (h)
κ_h	—	feed conductivity (S/cm)
κ_c	—	distillate conductivity (S/cm)
S'	—	indicator describing the degree of field synergy
C_h	—	feed solution concentration (g/L)
C_c	—	out solution concentration (g/L)
C_r	—	internal resistance factor
κ_h	—	feed solution conductivity (S/cm)
κ_c	—	out solution conductivity (S/cm)
u,v,w	—	velocity in the x, y, z direction (m/s)
u_i	—	velocity in the i direction (m/s)
η	—	viscosity coefficient
P	—	pressure (MPa)
ρ	—	density (g/m^3)
F_x, F_y, F_z	—	quality force on microelement in the x, y, z direction (m/s^2)
c_P	—	specific heat capacity (J/kg·K)
k	—	thermal conductivity (w/m^2·K)
T	—	temperature (K)
S_T	—	heat energy converted by fluid mechanical energy due to viscosity (J/kg)
λ	—	molecular average free path (m)
K_B	—	Boltzmann constant
T	—	average temperature on both membrane sides (K)
σ	—	molecule diameter (m)
r	—	radius (m)
ε	—	membrane porosity

τ	—	tortuosity factor
δ	—	membrane thickness (mm)
M	—	molecular molar weight of the components through the membrane (g/mol)
R	—	gas constant (kJ/kmol·K)
T_m	—	average temperature (K)

Acknowledgements

This study was supported by the National Nature Science Foundation of China (No. 20806008) and the National Nature Science Foundation of China (No. 21111120074).

References

[1] F. Banat, S. A1-Asheh, Q.M. Taishat, Treatment of waters colored with methylene blue dye by vacuum membrane distillation, Desalination 174 (2005) 87–96.
[2] A. Criscuoli, J. Zhong, A. Figoli, M.C. Carnevale, R. Huang, E. Drioli, Treatment of dye solutions by vacuum membrane distillation, Water Res. 42 (2008) 5031–5037.
[3] M.S. EL-Bourawi, M. Khayet, R. Ma, Z. Ding, Z. Li, X. Zhang, Application of vacuum membrane distillation for ammonia removal, J. of Mem. Sci. 301 (2007) 200–209.
[4] S. Al-Asheh, F. Banat, M. Qtaishat, M. Al-Khateeb, Concentration of sucrose solutions via vacuum membrane distillation, Desalination 195 (2006) 60–68.
[5] Z.P. Zhao, F.W. Ma, W.F. Liu, D.-Z. Liu, Concentration of ginseng extracts aqueous solution by vacuum membrane distillation (1) Effects of operating conditions, Desalination 234 (2008) 152–157.
[6] S.D. Hananjay, K.S. Kamalesh, Desalination of brine and produced water by direct contact membrane distillation at high temperatures and pressures, J. of Memb. Sci. 389 (2012) 380–388.
[7] F. Stephanie, K.S. Kamalesh, A mathematical model of an aqueous–organic partition-based controlled release system using microporous membranes, J. Controlled Release 61 (1999) 345–360.
[8] F. Stephanie, K.S. Kamalesh, Mathematical model of a hybrid dispersed network-membrane-based controlled release system, J. Controlled Release 70 (2001) 51–61.
[9] X.Y. Wang, L. Zhang, H.J. Yang, H.L. Chen, Feasibility research of potable water production via solar-heated hollow fiber membrane distillation system, Desalination 247 (2009) 403–411.
[10] M. Jean-Pierre, L. Stéphanie, Corinne Cabassud Vacuum membrane distillation of brine reverse osmosis brines, Water Res. 44 (2010) 5260–5273.
[11] A.M. Alklaibi, N. Lior, Transport analysis of air-gap membrane distillation, J. Membr. Sci. 255 (2005) 239–253.
[12] A.M. Alklaibi, N. Lior, Heat and mass transfer resistance analysis of membrane distillation, J. Membr. Sci. 282 (2006) 362–369.
[13] M. Qtaishat, T. Matsuura, B. Kruczeka, M. Khayet, Heat and mass transfer analysis in direct contact membrane distillation, Desalination 219 (2008) 272–292.
[14] Z.Y. Guo, D.Y. Li, B.X. Wang, A novel concept for convective heat transfer enhancement, Int. J. Heat Mass Transfer 41 (1998) 2221–2225.
[15] Z.Y. Guo, S. Wang. Novel concept and approaches of heat transfer enhancement, in: P. Cheng (Ed.), Proc. of Symposium on Energy and Engineering, Hong Kong, 2000, New York, Begel House, 2000, 11–15.
[16] D.L. Gao, Master thesis, A Preliminary Study of Field Synergy on Treatment of Brine Using Vacuum Membrane Distillation. Beijing Institute of Technology, Beijing, 2011.
[17] X.S. Wang, Reverse Osmosis Membrane Technology and its Application in Chemical Industry and Environmental Protection, Chemical industry press, Beijing, 1988.
[18] J. Shi, Q. Yuan, C.J. Gao. Membrane Technology Handbook, Chemical Industry Press, Beijing, 2001.